ACCURATE AND RELIABLE DETERMINATION OF EDGE AND VERTEX STRESS INTENSITY FACTORS
IN THREE-DIMENSIONAL ELASTOMECHANICS

Börje Andersson and Urban Falk
Structures Department
The Aeronautical Research Institute of Sweden (FFA)
P.O. Box 11021, S-161 11 Bromma, Sweden

Ivo Babuška
Institute for Physical Science and Technology
University of Maryland
College Park Maryland, U S A

Abstract

The paper describes how to derive accurate and reliable solutions to the equations of three-dimensional elastomechanics on domains of general shape. Use of the proposed computational procedures makes it possible to efficiently perform the three-dimensional fracture mechanics analyses needed for damage tolerance design of aircraft structures.

The h-p version of the finite element is the numerical method employed. The exact solution may close to edges and vertices be expanded in series. The terms in the series consists of unknown constants and functions which characterize the solution in areas where crack nucleation and propagation often takes place. Under certain conditions these constants may be used to predict growth and unstable fracture in metals and ceramic materials. For edges we develop a new method for calculation of polynomial approximations to the mode I, mode II and mode III edge intensity functions. For vertices we define intensity parameters named vertex intensity factors and vertex-edge intensity factors. Computational procedures are developed with which all intensity parameters can be determined with an error which decreases exponentially with increasing number of degrees of freedom. Numerical examples demonstrating the reliability and accuracy obtainable when solving three-dimensional problems are given.

1 Introduction

Damage tolerant design and fatigue design are analytical procedures. Component testing and full scale testing are required to verify the analytical procedure used. Application of the MIL-A-83444 design code for damage tolerant design requires that designers safely should predict the growth of three-dimensional cracks in complex aircraft components. The prediction of stable slow crack growth and the onset of unstable crack growth are in practical cases based on a linear elastic fracture mechanics analyses. Effects of

material non-linearities due to high loads in the load spectrum are considered in the crack growth analysis by use of socalled crack retardation models.

Over the past decade it has been possible to solve three-dimensional linear elastic fracture mechanics problems using the finite element method. The time-consuming task of creating three-dimensional meshes has however prevented routinely use of these methods in the damage tolerance analysis of aircraft structures. Further the reliability of the numerical methods available which not always is satisfactory has only recently been adresses in the engineering community (see for example (1) and references therein). The accuracy of the computed data depend on the properties of the exact solution and the finite element method used.

In this paper a computational procedure with which three-dimensional linear elastic fracture mechanics problems routinely may be solved in a reliable way is devoloped. All fracture mechanics parameters (including also vertices) may be extracted from the finite element solution with an error which decreases exponentially with increasing number of degrees of freedom used.

2 Differential equations

We consider a domain V' (for example see Figure 1) which is a union of subdomains $V^{(i)}$. The surface of each subdomain $V^{(i)}$ is a union of piecewise analytical subsurfaces $S^{(i)}$ (a function is said to be analytic if all derivatives are finite and the function can be expanded in a Taylor series). Two or more subsurfaces $S^{(i)}$ intersect at edges $\gamma^{(j)}$ at a constant angle $\omega^{(j)}$. The edges $\gamma^{(j)}$ form piecewise smooth (at least C^1 continous) curves in R^3. An edge $\gamma^{(j)}$ is either closed or terminates at two vertices. Nonclosed edges start and end at a vertex. Vertices are labelled $A^{(k)}$.
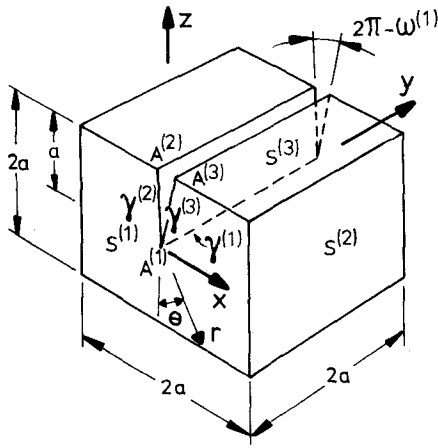
Figure 1 Cube-shaped domain with edge-crack

and stresses may be found. In practical design, the main objective often is to derive precise information about the behaviour of the solution in the neighbourhood of vertices and edges.

The domain $\bar{V} = V \cup S$ has in each subdomain linearly elastic material properties. The strain-displacement relations are for linear kinematics given by equation (1). The equilibrium equations are given by equations (2). For an isotropic material the constitutive equation are defined by the equations (3) in which μ and G are Lame's constants. For an anisotropic material the constitutive equations are given by equation (4).

$$\varepsilon_{ij} = \frac{1}{2}(u_{i,j} + u_{j,i}) \qquad (1)$$

$$\sigma_{ij,j} + X_i = 0 \qquad (2)$$

$$\sigma_{ij} = \mu\delta_{ij}\varepsilon_{kk} + 2G\varepsilon_{ij} \qquad (3)$$

$$\sigma_{ij} = C_{ijkl}\varepsilon_{kl} \qquad (4)$$

The Latin indices take the values in the set {1,2,3}. The usual summation convention is used. δ_{ij} is the Kronecker symbol. $\sigma_{ij}, \varepsilon_{ij}$ and u_i are cartesian stress, strain and displacement components respectively.

From the equations (1)-(3) the Navier equations (for isotropic materials) in the unknown displacement field u_i are obtained as,

$$Gu_{i,jj} + (\mu+G)u_{j,ii} + X_i = 0 \qquad (5)$$

For an anisotropic material the corresponding equations are,

$$C_{imlj}u_{j,lm} + X_i = 0 \qquad (6)$$

Boundary conditions considered are prescribed homogenous displacements on $S_u \subset S$ and prescribed surface tractions T_i on $S_T \subset S$, that is

$$u_i = 0 \qquad \text{on } S_u \qquad (7)$$

and

$$T_i = \sigma_{ij}\nu_j \qquad \text{on } S_T \qquad (8)$$

where ν_j is outward normal to S_T.

The tractions T_i are assumed to be zero close to edges and vertices where intensity factors/functions are to be computed. We assume that the tractions or displacements which are prescribed on $S^{(i)}$ are analytid on $\bar{S}^{(i)}$ and similarily X_i are assumed to be analytic on $\bar{V}^{(i)}$.

Denote by $^0H^1(V)$ the Sobolev space,

$$^0H^1(V) = \{u_i \subset H^1(V) \,|\, u_i = 0 \text{ on } S_u\} \qquad (9)$$

The exact solution to the equations (6) with boundary conditions (7) and (8) is the minimizer of the quadratic functional $F(u)$ over $^0H^1(V)$, where

$$F(u) = 1/2B(u,u) - Q(u) \qquad (10)$$

with

$$B(u,u) = \int_V C_{imlj}u_{j,l}u_{i,m} \, dV \qquad (11)$$

$$Q(u) = \int_V u_i X_i dV + \int_{S_T} u_i T_i dS \qquad (12)$$

The strain energy in the system is $1/2B(u,u)$.

3 Properties of exact solution

The properties of the exact three-dimensional solution to the Navier equations under conditions defined in section 2 will briefly be reviewed. We know that there exists only one solution (determined except for a rigid body motion) which has finite energy (this solution we are seeking). This solution is analytic everywhere on $\bar{V}$ except on the edges. The solution is singular (singular imply that some derivates are unbounded) along the edges and at the vertices.

The character of the solution can be discussed in the way that the solution is split into the singular part and the regular part (regular imply that all derivatives up to a given degree are bounded). The singular behaviour is different along the open edges (ie excluding the vertices) and in the neighbourhood of the vertices.

Consider first, the behaviour of the exact solution close to smoothly curved open edge $\gamma^{(j)}$ (Figure 2). A detailed mathematical treatment is given in [5,6].

The edge is for clearity assumed to be located in one plane z=0 in a local cartesian coordinate system. The two faces terminating at the edge $\gamma^{(j)}$ are assumed to be stressfree and intersect at a constant angle $\omega^{(j)}$ along the edge. A local curvilinear coordinate system (x_1,x_2,x_3) which is fixed to the edge $\gamma^{(j)}$ where the x_1-axis is located in the plane of the edge perpendicular to the edge is used to characterize the behaviour of the exact solution close to the crack front.
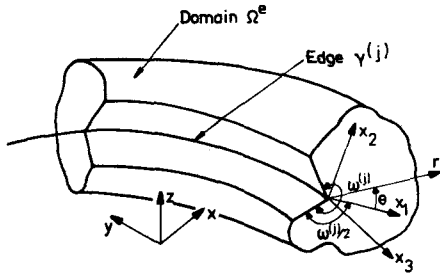
1731

Figure 2 Edge $\gamma^{(j)}$ located in plane z=0 in a local Cartesian xyz-system

The displacements in the x_i-direction may close to the edge (for noninteger λ) be written in the form,

$$u_i = \frac{\sqrt{2\pi}}{G} \sum_{m=1}^{M} \left[K_I^{(m)}(x_3) \times r^{\lambda_I^{(m)}} \times \Psi_{Ii}\left(\theta, \lambda_I^{(m)}\right) + \right.$$

$$K_{II}^{(m)}(x_3) \times r^{\lambda_{II}^{(m)}} \times \Psi_{IIi}\left(\theta, \lambda_{II}^{(m)}\right) +$$

$$\left. K_{III}^{(m)}(x_3) \times r^{\lambda_{III}^{(m)}} \times \Psi_{IIIi}\left(\theta, \lambda_{III}^{(m)}\right) \right]$$

$$+ U_i(r,\theta,x_3) \tag{13}$$

where U_i are functions of higher smoothness. The value M depends in general on the imposed load and the neighbourhood we seek the solution as well as required accuracy.

In equation (13) $\lambda_I^{(m)}$, $\lambda_{II}^{(m)}$, $\lambda_{III}^{(m)}$ are the edge eigenvalues and $\Psi_{Ii}^{(m)}$, $\Psi_{IIi}^{(m)}$ and $\Psi_{IIIi}^{(m)}$ the corresponding edge eigenfunctions. For exceptional angles $\omega^{(j)}$ the eigenvalues $\lambda^{(m)}$ may be integers or multiple. In these cases we can have additional terms of the type $r^{\lambda}(\ln r)^q$ too. For complex eigenvalues λ we take the real and the imaginary parts which corresponds to an oscillatory behaviour of the stresses.

The angular functions Ψ_{Ii}, Ψ_{IIi} and Ψ_{IIIi} are for isotropic materials,

$$\Psi_{I1} = [\kappa - Q_1(\lambda_I^{(m)}+1)]\cos(\lambda_I^{(m)}\theta) - \lambda_I^{(m)}\cos[(\lambda_I^{(m)}-2)\theta]$$

$$\Psi_{I2} = [\kappa - Q_1(\lambda_I^{(m)}+1)]\sin(\lambda_I^{(m)}\theta) + \lambda_I^{(m)}\sin[(\lambda_I^{(m)}-2)\theta]$$

$$\Psi_{I3} = 0$$

$$\Psi_{II1} = [\kappa + Q_2(\lambda_{II}^{(m)}+1)]\sin(\lambda_{II}^{(m)}\theta) -$$
$$\lambda_{II}^{(m)}\sin[(\lambda_{II}^{(m)}-2)\theta]$$

$$\Psi_{II2} = -[\kappa - Q_2(\lambda_{II}^{(m)}+1)]\cos(\lambda_{II}^{(m)}\theta) -$$
$$\lambda_{II}^{(m)}\cos[(\lambda_{II}^{(m)}-2)\theta] \tag{14}$$

$$\Psi_{II3} = 0$$

$$\Psi_{III1} = 0$$

$$\Psi_{III2} = 0$$

$$\Psi_{III3} = \sin(\lambda_{III}^{(m)}\theta)$$

where

$\kappa = 4 - 3\mu$ (conditions equivalent to plane strain conditions apply close to crack-tip) and

$$Q_1 = -\frac{1-\lambda_I^{(m)}}{1+\lambda_I^{(m)}} \frac{\sin\left[\omega(1-\lambda_I^{(m)})/2\right]}{\sin\left[\omega(1+\lambda_I^{(m)})/2\right]}$$

$$Q_2 = \frac{\sin\left[\omega(1-\lambda_{II}^{(m)})/2\right]}{\sin\left[\omega(1+\lambda_{II}^{(m)})/2\right]} \tag{15}$$

The functions $K_I^{(m)}$, $K_{II}^{(m)}$ and $K_{III}^{(m)}$ are edge stress intensity functions which are basic design parameters used for example in damage tolerance design of aircraft structures [7].

For straight edges and isotropic materials, the edge eigenvalues $\lambda_I^{(m)}$ and $\lambda_{II}^{(m)}$ are roots to the two equations

$$\sin(\lambda\omega) \pm \lambda\sin(\omega) = 0 \quad . \tag{16}$$

The plus sign apply for mode I deformation and the minus sign for mode II deformation. The mode III eigenvalues are

$$\lambda_{III}^{(m)} = \pm\frac{m\pi}{\omega}, \quad m=1,2,3\ldots \tag{17}$$

Finite energy in the solution requires that all eigenvalues are non-negative. The solution $\{-\lambda^{(m)}, \Psi^{(m)}(\theta,-\lambda^{(m)})\}$ that also satisfies Navier equations is used in connection with extracting approximate values for the edge intensity functions $K(x_3)$ out of the finite element solution.

A mathematical description of properties of the exact solution close to a curved edge is presently not available. We expect, however that for a smooth edge which is curved in one plane the equation (13) have to be augmented with terms of the type [6]

$$\frac{\sqrt{2\pi}}{G} \sum_{m=1}^{M} \sum_{l=1}^{\infty} [k_I^{(m)}(x_3) \times r^{(\lambda_I^{(m)}+1)} \times \Psi_{Iilm}\left(\theta, \lambda_I^{(m)}\right) +$$

$$k_{II}^{(m)}(x_3) \times r^{(\lambda_{II}^{(m)}+1)} \times \Psi_{IIilm}\left(\theta, \lambda_{II}^{(m)}\right) +$$

$$k_{III}^{(m)}(x_3) \times r^{(\lambda_{III}^{(m)}+1)} \times \Psi_{IIIilm}\left(\theta, \lambda_{III}^{(m)}\right)]$$

$$\tag{18}$$

The functions ψ_{Iilm} etc depend only on the curvature of the crack front. A new set of intensity functions $(k_I^{(m)}(x_3) \ldots)$ thus can be defined. Since $\lambda > 0$ and $1 \geq \bar{1}$ the terms in the equation (18) correspond to finite stresses at the edge. For the curved edge, equation (13) thus apply with M=1.

The edge intensity functions are, for smooth loading and a smoothly shaped edge, smooth functions in the coordinate x_3. This property will in section 7 be used to derive polynomial approximations to the edge stress intensity functions on the interior of the edge $\gamma^{(j)}$.

The tractions in the local (x_1, x_2, x_3)-system corresponding to displacements given by the equations (13) are,

$$T_i = \sum_{m=1}^{M} \left[K_I^{(m)}(x_3) \times \lambda_I^{(m)} \times r^{(\lambda_I^{(m)}-1)} \times X_{Ii}(\theta, \lambda_I^{(m)}) + \right.$$
$$K_{II}^{(m)}(x_3) \times \lambda_{II}^{(m)} \times r^{(\lambda_{II}^{(m)}-1)} \times X_{IIi}(\theta, \lambda_{II}^{(m)}) + \qquad (19)$$
$$K_{III}^{(m)}(x) \times \lambda_{III}^{(m)} \times r^{(\lambda_{III}^{(m)}-1)} \times$$
$$\left. X_{IIIi}(\theta, \lambda_{III}^{(m)}) \right] + \text{smoother terms}$$

Consider now the behaviour of the exact solution close to a vertex $A^{(K)}$ at which J straight edges terminates (compare Figure 1). Material properties are assumed to be isotropic. The solution close to the edges is given by equation (13). Near the vertex the x_i-displacement is [5]

$$\sum_{m=1} S^{(m)} \rho^{\Lambda^{(m)}} \cdot W_i^{(m)}(\phi, \theta) + \text{smoother terms} \qquad (20)$$

In the case when Λ is integer or multiple equation (20) has possibly to be augmented with terms of the type $\rho^\Lambda (\ln\rho)^q$ (q integer). In the equation (20) the parameter $\Lambda^{(m)}$ is the vertex eigenvalue of order m and (ρ, ϕ, θ) are spherical coordinates. The maximum number of terms depends on the loading. In engineering applications the number of terms may be set large. This is of practical importance since several terms might be needed to characterize the solution [8].

The functions $W_i^{(m)}(\phi, \theta)$ which can be understood as being defined on the spherical surface $\rho=1$ have a singular behaviour for angles (ϕ, θ) where edges intersect with the spherical surface.

The functions $W_i^{(m)}(\phi, \theta)$ may be decomposed into a regular and a singular part. The advantage is that the singular character of the solution at the *vertex* can be characterized by a few intensity factors. These intensity factors may eventually, as in standard linear elastic fracture mechanics, be used to predict growth and unstable fracture [7].

If for clearity only the first term in the series (20) is considered the decomposed solution can for non-integer Λ be written

$$u_i = \chi(\rho) \cdot S^{(1)} \cdot \rho^{\Lambda^{(1)}} \cdot V_i^{(1)}(\phi, \theta) + \frac{\sqrt{2\pi}}{G} \sum_{j=1}^{J} \chi(r_j) \cdot \sum_{k=1}$$

$$\{ s_{Ij}^{(1,k)} \cdot \rho^{(\Lambda^{(1)} - \lambda_{Ij}^{(k)})} \cdot (r_j^{\lambda_{Ij}^{(k)}} \cdot \Psi_{Iij}(\theta_j, \lambda_{Ij}^{(k)})) + $$

$$s_{IIj}^{(1,k)} \cdot \rho^{(\Lambda^{(1)} - \lambda_{IIj}^{(k)})} \cdot (r_j^{\lambda_{IIj}^{(k)}} \cdot \Psi_{IIij}(\theta_j, \lambda_{IIj}^{(k)})) + $$

$$s_{IIIj}^{(1,k)} \cdot \rho^{(\Lambda^{(1)} - \lambda_{IIIj}^{(k)})} \cdot (r_j^{\lambda_{IIIj}^{(k)}} \cdot \Psi_{IIIij}(\theta_j, \lambda_{IIIj}^{(k)})) \}$$

+ smoother terms   (21)

where r_j is the distance to edge j. The functions χ are cut-off functions infinitely smooth with function values 1 for $\rho=0$ and $r_j=0$ and value 0 at a distance from the vertex and the edges respectively.

The function V_i in equation (21) is a smooth function and identical to W_i in equation (20) except for the neighbourhood of the edges.

The scalar $S^{(1)}$ which depends on the loading we name the *vertex intensity factor* of order 1. The vertex intensity factor S may be used to generally characterize the solution at the vertex. Close to the vertex and first order edge j the edge intensity function $K_{Ij}^{(1)}$ is for nonzero $s_{Ij}^{(1,1)}$ obtained from equations (13) and (21) as

$$K_{Ij}^{(1)}(\rho) = s_{Ij}^{(1,1)} \cdot \rho^{(\Lambda^{(1)} - \lambda_{Ij}^{(1)})} + \text{smoother terms} \qquad (22)$$

Similar expressions apply for the mode II and mode III edge intensity functions close to a vertex.

The scalar $s_{Ij}^{(1,1)}$ we name the mode I *vertex-edge* intensity factor of order 1 for edge j terminating at vertex $A^{(k)}$. Dependent on actual values of Λ and λ the edge intensity function may be zero, finite or infinite at a vertex.

The equation (22) was discussed in an engineering context in [9] and was given in a very general setting in [5].

If one of the edges is curved in one plane the equation (20) has to be augmented with terms of the type $\rho^{\Lambda+k}$ with k=1,2,3... . The equations (21) and (22) then apply for a curved crack front too. For integer values of Λ the series (20) must be augmented with terms $\rho^\Lambda (\ln\rho)^q$.

The vertex eigenvalues Λ and the functions $W_i^{(m)}(\phi, \theta)$ must in all practical situations be determined numerically. A accurate and reliable procedure to do this is described in section 6.

1733

Here we apply the h-p version of the finite element method for solving the minimization problem defined by the equations (9) - (12). In the h-p version of the finite element method convergence is obtained by simultaneously decreasing the element sizes and increasing the polynomial order of approximation p. The h-p version has exponential rate of convergence in energy with respect to the number of degrees of freedom N, eg [2, 4], that is

$$B(\tilde{u}-\tilde{\tilde{u}},\tilde{u}-\tilde{\tilde{u}}) = B(\tilde{u},\tilde{u})-B(\tilde{\tilde{u}},\tilde{\tilde{u}}) \leq C_1 . e^{-C_2.\sqrt{N}} \qquad (23)$$

where $B(*,*)$ is defined in equation (10). The polynomial order of approximation is p and C_1 and C_2 are constants independent of p. The methods developed in the present paper for calculation of different intensity functions are all constructed as to give an exponential decrease in error in computed data when used in combination with the h-p version of FEM.

For one- and two-dimensional problems it was shown in [3] that the optimal mesh close to a singularity is graded in geometric progression with a grading factor α of about 0.15. Numerical analyses of three-dimensional problems using meshes strongly graded towards vertex and edges have been found to give an exponential decrease in the energy error [10]. For three-dimensional problems the optimal p-distribution in the mesh has to be defined. In connection with the model problems analysed in section 10, the effect of mesh design close to edges and vertices will be exemplified.

The finite element program STRIPE which is used to derive numerical data in the present paper i based on the h-p version of the finite element method. Trial functions used are formed as tensor products $H_1(\xi_1)H_m(\xi_2)H_n(\xi_3)$ as suggested in [11]. For a brick-shaped finite element for example

$$H_0(\xi_i) = \frac{1}{2}(1-\xi_i), \quad H_1(\xi_i)=\frac{1}{2}(1+\xi_i)$$

$$H_k(\xi_i) = \begin{cases} \dfrac{1}{k!}(\xi_i^k-1) & k \text{ even} \\ \\ \dfrac{1}{k!}(\xi_i^k-\xi_i) & k \text{ odd} \end{cases} \qquad k>1 \qquad (24)$$

with $0 \leq l \leq p$, $0 \leq m \leq p$, $0 \leq n \leq p$ and $l+m+n \leq p+2$

where p is polynomial order of approximation.

For a uniform order of approximation the number of degrees of freedom for an element is

$$\frac{(p+1)(p+2)(p+3)}{6} + 3(p+1). \qquad (25)$$

The approximation corresponds to complete polynomials of order p together with $3(p+1)$ monomial terms of degree higher than p.

Use or self-adaptive solution schemes may under certain conditions significantly reduce the computational effort needed to derive solutions of required accuracy. One might argue that an adaptive process itself may not add much to the strong convergence already obtained when employing the h-p version of FEM. In many practical situations, however, users provide (of different reasons) very non-optimal meshes. For such cases the p-adaptive solution scheme discussed here may be very efficient as demonstrated in section 10 (see also [10]).

By p-adaptive we here mean that finite elements in a fixed mesh automiatically are assigned different orders of approximation p in a near-optimal way.

Instead of directly minimizing the computational effort needed most adaptive schemes are designed to minimize the dimension (that is the number of degrees of freedom) of the trial space used. This approach may be justified due to the strong relation between the number of degrees of freedom and the time needed to solve the resulting set of equations (which is the major effort in most FE-analyses).

The construction of new trial spaces of low dimension thus is the crucial part in the adaptive process. For each trial function which is a candidate to be used to expand the existing trial space, efficiency indices called error indicators need be calculated [10,12,13]. An error indicator is an estimate of the decrease in error in energy, stress or stress intensity factor etc that will be obtained if the existing trial space is expanded with the actual trial function.

If the candidate trial function describing the x_i-displacements is denoted v_i the error indicator used, is (i is fixed)

$$\eta_i^2 = \left| \int_\Omega v_i r_i d\Omega \right|^2 / \int_\Omega C_{ijil}v_{i,1}v_{ij} \, d\Omega \qquad (26)$$

with the residual

$$r_i = C_{imlj}\tilde{u}_{j,lm} \qquad (27)$$

where $\tilde{u}$ is the finite element solution.

This indicator [10,12,13]) is an estimate of the change in energy norm when adding the trial function v_i to existing trial space.

The error in computed vertex and edge intensity factors depend on the error in energy norm for the primary and an auxiliary load system [10]. Error indicators which are estimates of the decrease in energy in the solution thus indirectly are measures of the decrease of the error in calculated intensity factors.

Denote by $^{(i)}N$ the dimension of the trial space $^{(i)}S^{(p)}$ at iteration i where p is the maximum

polynomial order or approximation used in any finite element. The space $\bar{S}^{(p)}$ of dimension $\bar{N}^{(p)}$ contains all trial functions of order p or less (equations (24) and (25)).

The main steps in the adaptive process used here are,

1 Set iteration number $i=1$ and $^{(1)}S = \bar{S}^{(2)}$

2 Calculate terms in element stiffness matrices and element load vectors which are related to the trial functions $v_i \in {}^{(i)}S$ and $v_i \in {}^{(i-1)}S$ ($^{(0)}S$ is the null space)

3 Assemble stiffnesses and solve the resulting system of linear equations using a domain solution technique

4 Calculate stresses and intensity parameters

5 If the number of iterations i have reached a preset value stop here

6 Calculate error indicators η_i^2 for all trial functions $v_i \in \bar{S}^{(i+2)}$ and $v_i \in {}^{(i)}S$

7 Determine $^{(i+1)}N$ and $^{(i+1)}S$ from values of error indicators and a few heuristic rules [7]

8 Set $i = i+1$ and continue at point 2

6 The fundamental eigenvalue problem

The vertex eigenvalues $\Lambda^{(m)}$ (equation (20)) can be determined analytically only for very degenerated cases. Numerical methods have to be used. The method developed here is well integrated with standard finite element techniques.

Consider the case when J straight edges terminates at a vertex $A^{(k)}$. Material properties are assumed isotropic. We know that the solution is of the form $\rho^\Lambda(\phi,\theta)$ (equation (20)). Solutions of this type satisfy (also for Λ integer)

$$\frac{\partial u_i}{\partial \rho} = \Lambda u_i/\rho \qquad (28)$$

The eigenvalues may be real or complex because we deal with a nonselfadjoint problem.

The problem of finding the lowest eigenvalue $\mathrm{Re}(\Lambda^{(1)}) > -1/2$ (for finite energy) is the fundamental eigenvalue problem. The solution we are seeking satisfy equation (6) with boundary conditions (8). At the vertex we have (equation (20) with $\rho=0$)

$$u_i = 0 \qquad . \qquad (29)$$

In order to determine the vertex eigenvalue we consider a spherical domain with radius ρ_u located symmetrically around the vertex $A^{(k)}$ (one such domain is shown in Figure 3).
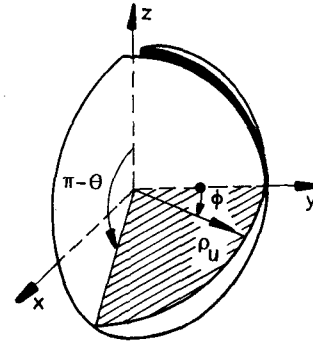

Figure 3   Subdomain Ω^e with spherical surface used for determination of vertex eigenvalues $\Lambda^{(m)}$

We use the weak form of the Navier equations and apply equation (28) as boundary condition on the spherical part of the surface of the subdomain to find approximative values for the vertex eigenvalues $\Lambda^{(m)}$.

The strain-displacement relations may using equations (1) and (28) be written in the form

$$\varepsilon_{kl} = (\Lambda/\rho_u) \times D_{kli} \times u_i + F_{klij} \times \partial u_i/\partial x_j \qquad (30)$$

where u_i and ε_{kl} are Cartesian displacements and strains respectively. The elements of the functions D_{kli} and F_{klij} depends on (ϕ,θ) only. The constitutive equations (30) which satisfy the constraint (28) are obtained by transforming the equation (1) to spherical coordinates (ρ,ϕ,θ) and replacing all derivatives $\partial/\partial\rho$ using equation (28) before transforming the resulting equations back to Cartesian coordinates, displacements etc.

The exact solution to the vertex eigenvalue problem is the minimizer to the functional defined by equation (10) with B(u,u) from (11) and with

$$Q(u) = \int_{\Gamma_s} u_k v_l \{ (\Lambda/\rho_u)\mu\delta_{kl} D_{mmi} + 2GD_{kli}) u_i +$$
$$(\mu\delta_{kl} F_{mmij} + 2GF_{klij}) \partial u_i/\partial x_j \} dS$$
$$(31)$$

The equations (10),(12) and (31) constitutes our eigenvalue problem. We use the standard finite element techniques to derive aproximative solutions $\hat{\Lambda}$ to Λ. The finite dimensional trial space used is for brick-shaped finite elements spanned by basis functions of the type given by equations (24). For wedge shaped finite elements similar shape-functions are used.

In matrix notation the resulting algebraic eigenvalue problem may be written.

$$[K]\{u\} = (\Lambda/\rho_u)[B]\{u\} + [B_{12}]\{u\} \qquad (32)$$

where $[K]$ is the ordinary stiffness matrix (as in linear elasto-statics) for the three-dimensional spherical subdomain considered, $[B]$ is a symmetric

positive definite matrix, $[B_{12}]$ is a non-symmetric matrix and $\{u\}$ is the vector with generalized degrees of freedom.

The matrices $[B]$ and $[B_{12}]$ are very sparse. By using so-called static condensation of the $[K]$-matrix the dimension of the algebraic eigenvalue problem (32) is significantly reduced. The computational effort needed for the static condensation is taken advantage of by using a domain solution scheme when solving the Navier equation on the entire domain.

The eigenvalues Λ may be real or complex. Complex eigenvalues appears in pairs which are complex conjugated.

For the numerical method devised here, theoretical convergence properties are known and used to aposteriori estimate the error in computed vertex eigenvalues. If the p-version of the finite element method is applied, the error in calculated eigenvalue is bounded by [14]

$$|\Lambda^{(m)} - \tilde{\Lambda}^{(m)}| \leq C_3 \times p^{-4 \min(\lambda^{(1)}, \Lambda^{(1)} + 1/2)} \qquad (33)$$

where λ is the minimum edge eigen value for edges terminating at the vertex and C_3 is a constant dependent on mesh and mapping function but independent of order of approximation p. The equality sign apply for p large.

The equation (33) may for p sufficiently large be used as an error estimate. From three solutions for different orders of approximation p the constant C_3, the exponent (which theoretically is $-4 \min(\lambda, \Lambda + 1/2)$) and Λ may be calculated by solving the set of three nonlinear equations. Practical experience shows that very sharp error estimates are obtained already for $p > 3$.

Finite energy in the solution requires that $\Lambda^{(1)} > -1/2$. The equation (32) give solutions $\Lambda^{(m)}$ with finite energy. There are solutions having infinite energy. Such solutions plays an important role in extraction of vertex and vertex-edge intensity factors (Sections 8 and 9).

It can be shown that if $\Lambda^{(m)} > -1/2$ is a solution then $-(\Lambda^{(m)} + 1)$ is a solution too. The corresponding eigenvector can be determined numerically from equation (32) by transposing the $[B_{12}]$-matrix and solving for $\{u\}$.

7 Extraction of edge intensity functions K

We consider the computation of the mode I, mode II and mode III edge intensity functions $K_I^{(m)}(x_3)$, $K_{II}^{(m)}(x_3)$ and $K_{III}^{(m)}(x_3)$ of different orders m on the interval $x_{31} \leq x_3 \leq x_{3u}$ (Figure 2).

The edge is defined by $x = X_e(t)$, $y = Y_e(t)$ and $z = 0$. The functions $X_e(t)$ and $Y_e(t)$ are assumed to be functions of high regularity on the interval $t_1 \leq t \leq t_u$. In practical cases the functions $X_e(t)$ and

$Y_e(t)$ may be trigonometric functions, polynomials etc. Blended function mapping [15] may be used to model edges of a general shape. The function $x_3(t)$, with unique inverse $t(x_3)$, should be smooth in order not to lower the convergence rate in the numerical solution process.

Edge intensity functions computation is based on the Betti reciprocity theorem,

$$\int_{\Gamma^e} ({}^{(1)}u_i \times {}^{(2)}T_i - {}^{(2)}u_i \times {}^{(1)}T_i) d\Gamma = \int_{\Omega^e} ({}^{(1)}u_i \times {}^{(2)}X_i -$$

$${}^{(2)}u_i \times {}^{(1)}X_i) \, d\Omega \qquad (34)$$

In equation (34) the left superindex refer to the load system considered. A left superindex (1) denotes the primary load system; a superindex (2) denotes an auxiliary load system selected to give small errors when extracting edge intensity data [9]. By a proper choice of the domain Ω^e and extraction functions ${}^{(2)}u_i$, it is possible to use equation (34) to determine the edge intensity functions of different orders m for mode I, mode II and mode III loading. This method is a generalization of the ideas given in [16] and [17].

The selection of the domain Ω^e for extraction of edge intensity functions is first discussed. Figure 4 schematically shows a subdomain $\Omega^e \subset R^3$ with surface $\Gamma_1 \cup \Gamma_2 \cup \ldots \cup \Gamma_6$ enclosing a part of the smooth edge. The surfaces Γ_1 and Γ_2 intersect at the edge at a constant angle ω. The surface Γ_3 is a cylinder with circular cross-section of radius ρ_1 and with its axis coinciding with the edge considered. The cylinder ends are labelled Γ_5 and Γ_6.
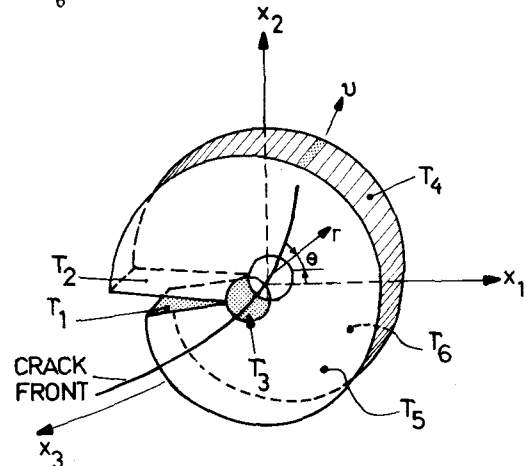

Figure 4   Domain Ω^e used for extraction of edge intensity functions.

The smoothness of the edge intensity functions (on the open interval) makes it possible to approximate them with polynomials. Subsequently the mode I stress intensity function of order m, $K_I^{(m)}$, may be approximated with the polynomial $\tilde{K}_I^{(m)}$ where,

$$\tilde{K}_I = \sum_{l=0}^{L} \tilde{k}_{Il} \times P_l(s) \qquad (35)$$

and

$$s = 2(t-t(x_{3l}))/(t(x_{3u})-t(x_{3l})) - 1 \qquad (36)$$

Analogous expressions are used for the mode II and mode III stress intensity function approximations. In equation (35) $\tilde{k}_{Il}^{(m)}$ are unknown coefficients to be determined and $P_l(s)$ are Legendre polynomials of order l. The reason for using Legendre polynomials, instead of ordinary polynomial terms, is that round-off errors will be reduced when computing the coefficients $\tilde{k}_{Il}^{(m)}$, $\tilde{k}_{III}^{(m)}$ and $\tilde{k}_{IIII}^{(m)}$. The number of terms $(L+1)$ in the series, equation (35), must be selected with care. Here $L=p$ is used where p is polynomial order of approximation used when employing the h-p version of the finite element method.

It can be shown that under general conditions the error in the coefficients $|K_{Il}^{(m)} - \tilde{K}_{Il}^{(m)}|$, $|K_{III}^{(m)} - \tilde{K}_{III}^{(m)}|$ and $|K_{IIII}^{(m)} - \tilde{K}_{IIII}^{(m)}|$ is of the same order as the error in the strain energy $(1\leq p)$ in the solution.

The extraction functions $^{(2)}u_i$ are defined as function of the curvilinear polar coordinates $(r,\theta,x_3(t))$, see Figure 2, where sections $x_3=$ constant form planes which are perpendicular to the edge. The relation between the local cartesian (x,y,z)-coordinates and the curvilinear $(r,\theta,x_3(t))$ coordinates is for curved edges not unique for large r.

In order to determine the coefficients $\tilde{k}_{Il}^{(m)}$, $\tilde{k}_{III}^{(m)}$ and $\tilde{k}_{IIII}^{(m)}$, $(L+1)$ extraction functions $^{(2)}u_i$ are needed. Dependent on the shape of the domain Ω^e used for extraction of edge intensity functions different extraction functions are used.

Figure 5 schematically shows different type of domains Ω^e which may be used for computation of vertex intensity factors $S^{(m)}$, vertex-edge intensity factors $s^{(m)}$ and edge intensity functions $K_I^{(m)}$, $K_{II}^{(m)}$ and $K_{III}^{(m)}$.

The domains A or F can be used for computation of vertex and vertex-edge intensity factors while the domains B,C,D or E may be used for computation of edge intensity functions.

For domains D,E and F the subsurfaces Γ_4, Γ_5 and Γ_6 normally are facetted where each facett is a face of a finite element. The domains B and C have a circular cross-section. Since the precise shape of each subdomain is defined by the finite element subdivision, so called blended function mapping [15] has to be used when adopting domains 'A', 'B' or 'C' for calculation of intensity parameters.

We briefly describe the case when the surfaces Γ_4, Γ_5 and Γ_6 of the domain Ω^e are of low regu-
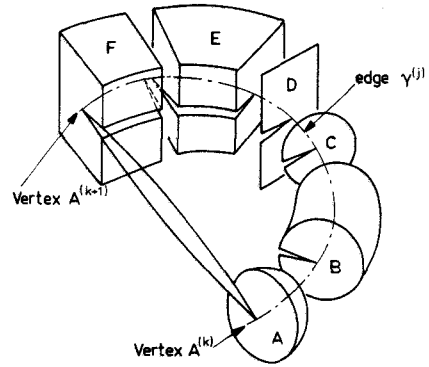

Figure 5   Domains Ω^e used for computation of edge intensity functions and vertex intensity factors for non-closed edge of elliptical shape

larity, (domain 'E' in Figure 5). The mapping from the local elements oriented coordinate system to the physical coordinate system may in this case be isoparametric. The ends Γ_5 and Γ_6 are not necessarily perpendicular to the edge considered.

The n'th extraction function of the in all $(L+1)$ functions needed for extraction of the mode I edge stress intensity function of order m is,

$$^{(2,n)}u_i = r^{-\lambda_I^{(m)}} \times \psi_{Ii}\left(\theta, -\lambda_I^{(m)}\right) \times Q_n(s) \qquad (37)$$

The coordinate s is defined by equation (36). For mode II and mode III similar expressions apply.

In equation (37) the functions $^{(2,n)}u_i$ are displacements in direction i in the curvilinear (x_1,x_2,x_3)-system which is fixed to the edge. For definition of the global displacements, the displacements of the edge are needed.

The displacements defined by equation (37) correspond for a vanishingly small radius r to the following tractions,

$$^{(2,n)}T_i = -r^{\left(-\lambda_I^{(m)}-1\right)} \times \lambda_I^{(m)} \times \chi_{Ii}\left(\theta, -\lambda_I^{(m)}\right) \times Q_n(s) \qquad (38)$$

The displacements $^{(2,n)}u_i$ correspond in the general case to nonzero volume forces $^{(2,n)}X_i$ and nonzero tractions $^{(2,n)}T_i$ on all subsurfaces Γ_1 to Γ_6.

The reciprocity theorem given by equation (5.2) may be rewritten as,

$$\int_{\Gamma_3} \left(^{(1)}u_i \times {}^{(2,n)}T_i - {}^{(2,n)}u_i \times {}^{(1)}T_i\right) d\Gamma =$$

$$\int_{\Omega^e} \left(^{(1)}u_i \times {}^{(2,n)}X_i\right) - \left(^{(2,n)}u_i \times {}^{(1)}X_i\right) d\Omega -$$

1737

$$\int_{\Gamma^e-\Gamma_3} \left[{}^{(1)}u_i \times {}^{(2,n)}T_i - {}^{(2,n)}u_i \times {}^{(1)}T_i \right] d\Gamma$$

$$(39)$$

By substituting ${}^{(2,n)}u_i$ from equation (37), ${}^{(2,n)}T_i$ from equation (38) and u_i from equation (13) for ${}^{(1)}u_i$ in the left hand side of equation (39) and shrinking the radius ρ_1 to zero, a set of equations in the unknown coefficients $\tilde{k}_{Il}^{(m)}$ are obtained.

The auxiliary load systems (left superindex (2)) have a strong singularity at the edge (see equation (38)). In the numerical implementation this will lead to severe cancellation of terms unless special care is taken. By subracting a displacement solution ${}^{(e)}u_i$ with the properties

$${}^{(e)}u_i(x_1,x_2,x_3) = {}^{(1)}u_i(0,0,x_3) \qquad (40)$$

from the primary load system when applying equation (39) the problem caused by cancellation may be avoided.

The displacement field defined by equation (40) implies that planes perpendicular to the crack front undergoes a pure translation. The corresponding edge intensity functions are identically zero. The corresponding surface tractions ${}^{(e)}T_i$ and volume forces ${}^{(e)}X_i$ are generally non-zero on Γ^e and Ω^e.

By applying the $(L+1)$ different extraction functions equation (37) and using $Q_n = P_n$ a set of linear equations in the unknown coefficients $\tilde{k}_{Il}^{(m)}$ is obtained,

$$[M]\{\tilde{k}\} = \{F\} \qquad (41)$$

Here $[M]$ is a symmetric square matrix of order $(L+1)$, $\{\tilde{k}\}$ and $\{F\}$ are vectors of length $(L+1)$. From equation (39) the elements in the matrix $[M]$ and in the vector $\{F\}$ are obtained as,

$$[M]_{l,n} = \beta \times \int_{x_{3l}}^{x_{3u}} P_l(x_3) \times P_n(x_3)\, dx_3$$

$$\begin{cases} = \beta \times \int_{x_{3l}}^{x_{3u}} P_l^2(x_3)\,dx_3 & \text{if } l = n \\[2mm] = 0 & \text{if } l \neq n \end{cases} \qquad (42)$$

$$\beta = -\lambda_I^{(m)} \int_{-\omega/2}^{\omega/2} [\psi_{Ii}(\theta,\lambda_I^{(m)}) \times \chi_{Ii}(\theta,-\lambda_I^{(m)}) +$$

$$\chi_{Ii}(\theta,\lambda_I^{(m)}) \times \psi_{Ii}(\theta,-\lambda_I^{(m)})]\,d\theta \qquad (43)$$

and

$$\{F\}_{,l} = \int_{\Omega^e} \left(({}^{(1)}u_i - {}^{(e)}u_i) \times {}^{(2,n)}X_i + {}^{(2,n)}u_i \times {}^{(e)}X_i \right)d\Omega - \qquad (44)$$

$$\int_{\Gamma^e-\Gamma_3} \left(({}^{(1)}u_i - {}^{(e)}u_i) \times {}^{(2,n)}T_i - {}^{(2,n)}u_i \times ({}^{(1)}T_i - {}^{(1)}T_i) \right) d\Gamma$$

The matrix $[M]$ is diagonal. Unique values of the coefficients $\tilde{k}_I^{(m)}$ are obtained. For calculation of $\tilde{k}_{III}^{(m)}$ and $\tilde{k}_{IIII}^{(m)}$ completely analogous expressions to equations (42) – (44) are obtained.

In the numerical computation of the edge intensity functions, the h-p version of the finite element method is used to derive approximate solutions to the problem studied. The finite element solution u_i then will be used as an approximation for ${}^{(1)}u_i$ and ${}^{(e)}u_i$. Based on the assumptions made in section 2, the volume forces ${}^{(1)}X_i$ are zero and the tractions ${}^{(1)}T_i$ are zero on the subsurfaces Γ_1 and Γ_2.

In the numerical computation of the vector $\{F\}$, first and second order derivatives of the finite element solution are needed. The second order derivatives needed are $\partial^2 u_i(0,0,t)/\partial t^2$ which for smooth crack fronts and smooth loading can be computed very accurately when employing the h-p version of the finite element method. The error in computed stress intensity functions will thus be governed by the error in computed first order derivatives of the finite element solution.

By a special choice of the domain Ω^e and the extraction functions ${}^{(2)}u_i$, it may be possible to construct expressions for the stress intensity functions such that first order derivatives of the displacements ${}^{(1)}u_i$ are not needed in the extraction process. A cylindrical domain where the subsurface Γ_4 is circular in a cross section perpendicular to the edge and where the ends Γ_4 and Γ_5 are perpendicular to the edge is an example of such a subdomain Ω^e (see domain labelled 'B' in Figure 5).

For subdomains Ω^e having this shape, the associated extraction functions for extraction of the mode I stress intensity function of order (m) are,

$${}^{(2,n)}u_i = f(r) \times r^{-\lambda_I^{(m)}} \times \psi_{Ii}(\theta,-\lambda_I^{(m)}) \times Q_n(s) \qquad (45)$$

where $f(r)$ is the function

$$f(r) = \begin{cases} 1 & r \leq \rho_1 \\[1mm] 1 - 3\left[\dfrac{r-\rho_1}{\rho_u-\rho_1}\right]^2 + 2\left[\dfrac{r-\rho_1}{\rho_u-\rho_1}\right]^3 & \rho_1 < r < \rho_u \\[1mm] 0 & r \geq \rho_u \end{cases}$$

$$(46)$$

suggested in [16].

The function $Q(s)$, with s from equation (36) is defined as to give zero tractions ${}^{(2,n)}T_i$ on the ends Γ_5 and Γ_6, eg

$$Q_n(s) = g(s) \times P_n(s) \tag{47}$$

with

$$g(s) = (1-s^2)^2 \tag{48}$$

The determination of the coefficients $\tilde{k}_{II}^{(m)}$, $\tilde{k}_{III}^{(m)}$ and $\tilde{k}_{IIII}^{(m)}$ respectively proceeds in a manner completely analogous to that descibed above for the case with more generally shaped subdomains Ω^e. The equation (41) still applies with the difference that the elements of the matrix [M] and the vector {F} are, different.

The advantage of using the extraction functions defined by equations (45)-(48) and a torodial domain Ω^e it that when evaluating the elements of the vector F only first and second order derivates of the function $u_i^{(e)}$, are needed for calculation of $T_i^{(e)}$ and $X_i^{(e)}$. Due to the smoothness of the function $u_i^{(e)}$, the error in the finite element approximation of $u_i^{(e)}$ decreases exponentially with increasing order of approximation p. Thus the quality of the finite element approximation of the stress intensity functions $K_I^{(m)}(x_3)$ etc. will only depend on the quality of a weighted average of the displacements inside the subdomain Ω^e.

8 Extraction of vertex intensity factors S

For calculation of vertex intensity factors $S^{(m)}$ of order m (equation (20)) we proceed basically as for calculation of edge intensity functions. The main difference is that extraction functions and eigenfunctions have to be determined numerically.

By applying the reciprocity theorem (34) on a subdomain of the type shown in Figure 3 or Figure 6 we arrive at explicit expressions for the vertex intensity factors.

For the subdomain shown in Figure 6 the subfaces Γ_1 and Γ_2 are traction free. The surface Γ_3 is spherical with radius ρ_u. The face Γ_s is facetted (Figure 6) or spherical (Figure 3).

The reciprocity theorem is

$$\int_{\Gamma_3} ({}^{(1)}u_i \times {}^{(2)}T_i - {}^{(2)}u_i \times {}^{(1)}T_i) d\Gamma =$$

$$-\int_{\Gamma_s} ({}^{(1)}u_i \times {}^{(2)}T_i - {}^{(2)}u_i \times {}^{(1)}T_i) d\Gamma \tag{49}$$

since extraction functions ${}^{(2)}u_i$ to be used have zero volume force density ${}^{(2)}X_i$.

The extraction function of order *m* is

$${}^{(2)}u_i = \rho^{-(\Lambda^{(m)}+1)} \times U_i^{(m)}(\phi,\theta) \tag{50}$$

where the functions $U_i^{(m)}(\phi,\theta)$ have to be determined numerically (see Section 6).
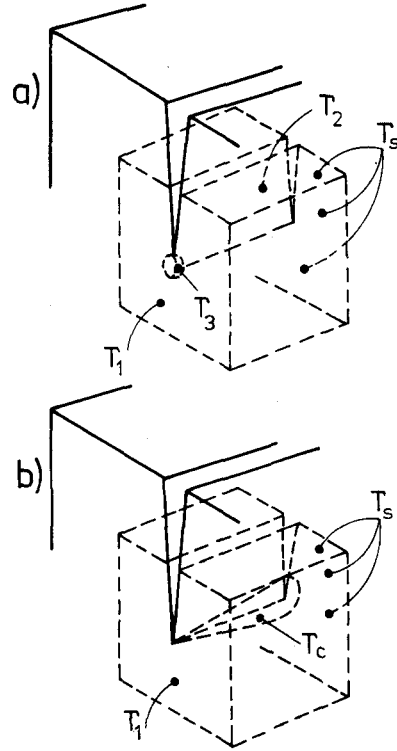

Figure 6 Example of subdomains used for extraction of vertex intensity factors (Figure a) and vertex-edge intensity factors (Figure b)

Approximations to the eigenfunctions $W_i(\phi,\theta)$ are determined from (32) up to an arbitrary constant multiplier $c^{(m)}$. The numerically determined function $\tilde{W}_i(\phi,\theta)$ is

$$\tilde{W}_i(\phi,\theta) = (c^{(m)}/\rho^\Lambda) \times \{H\}^T \times \{u\} \tag{51}$$

where {H} is a vector of basis functions, equations (24), evaluated at local coordinates ξ_i corresponding to points (ϕ,θ) on the spherical surface $\rho=\rho_u$.

It is necessary that the scaling parameter $c^{(m)}$ can be accurately determined from the numerical solution. The most accurate quantity in the numerical solution is, except for the Λ-value (equation (33)), the energy $1/2B(u,u)$ (equation (11)) in the solution. We define the scaling factor $c^{(m)}$ (and thus indirectly $S^{(m)}$) as

$$c^{(m)} = \frac{G \times \rho_u^{(2\Lambda^{(m)}+1)}}{1/2\{u\}^T[K]\{u\}} \tag{52}$$

where a right superindex T denotes transpose, G is the shear modulus and ρ_u the radius of the surface Γ_3 used in the finite element analysis. The matrix [K] and the vector {u} (for eigenvalue $\Lambda^{(m)}$) are those in equation (32).

The extraction function ${}^{(2)}u_i$ need not be scaled. The exact solution to the Navier equations is on the surface Γ_3 for small $\rho=\rho_\ell$ given by equation (20).

The calculation of the vertex intensity factor $S^{(m)}$ now proceeds in the following way. First approximations to the eigenfunctions $W_i^{(m)}(\phi,\theta)$ and the extractionfunctions $U_i^{(m)}(\phi,\theta)$ are determined numerically. The left-hand side of equation (49), which is independent of ρ_u (small) and contains only the unknown $S^{(m)}$ due to ortogonality properties between functions U_i and W_i, is then evaluated numerically.

The right hand side of equation (49) is evaluated by substituting the finite element solution for $^{(1)}u_i$ and $^{(1)}T_i$. Tractions are calculated using equations (30) in order to obtain a higher rate of convergence.

The resulting linear equation has the only unknown $S^{(m)}$.

9 Extraction of vertex-edge intensity factors

The mode I edge intensity function of order 1 for edge j may for ρ small be written (ρ is distance to the vertex)

$$K_{Ij}^{(1)}(\rho) = \sum_{m=1} s_{Ij}^{(m,1)} \, \rho^{(\Lambda^{(m)} - \lambda_{Ij}^{(1)})} \tag{53}$$

where $s_{Ij}^{(m,1)}$ are the mode I order 1 vertex-edge intensity factors for edge j.

Similar expressions apply for higher order edge intensity functions and also for the mode II and mode III edge intensity functions. For simplicity equations given in this section are for the mode I component.

The methods devised in Section 7 may be used to determine the edge-intensity functions close to a vertex provided that $\Lambda^{(1)} \geq \lambda_{Ij}^{(1)}$. For an edge intensity function of order n, the corresponding expression is $\Lambda^{(1)} \geq \lambda_{Ij}^{(n)}$. Since this condition is not always satisfied in practical situations a procedure for calculation of vertex-edge intensity factors is useful.

The computational procedure suggested proceeds as follows. First vertex eigenvalues $\Lambda^{(m)}$, vertex eigenfunctions $W^{(m)}(\phi,\theta)$ and vertex intensity factors $S^{(m)}$ are determined as described in Sections 6 and 8. Each vertex eigenvalue/eigenfunction (after scaling, equation (52)) are then treated separately by computing the corresponding vertex-edge intensity factors. The vertex-edge intensity factors for the load systems of interest (equation (53)) are finally obtained by superposition of fundamental solutions for each vertex eigenfunction (the vertex intensity factors $S^{(m)}$ are known).

For calculation of vertex-edge intensity factors we apply an extraction procedure similar to that used in Section 7. The extraction function used when considering edge j and mode I edge intensity functions of order k is (compare equation (37))

$$^{(2)}u_i = r_j^{-\lambda_{Ij}^{(k)}} \cdot \Psi_{Iij}(\theta_j, -\lambda_{Ij}^{(k)}) \tag{54}$$

where r_j is distance to edge j, $\lambda_{Ij}^{(k)}$ is the edge eigenvalue determined from equations (16) and Ψ_{Iij} is the edge eigenfunction from (14). The volume force density is $^{(2)}X_i=0$ and tractions $^{(2)}T_i=0$ are zero on subfaces terminating at edge j.

The domain Ω^e used for extraction of vertex-edge intensity factors are shown in Figure 6b. The edge Γ_S which is facetted in the figure may also be spherical.

The edge j and the vertex is not included in the subdomain Ω^e used. On the conical surface Γ_C (cone angle is vanishingly small) the solution for a single vertex eigenfunction of order m $W^{(m)}(\phi,\theta)$ considered is

$$u_i = \sum_{k=1} \hat{s}_{Ij}^{(m,k)} \cdot \rho^{(\Lambda^{(m)} - \lambda_{Ij}^{(k)})} \cdot \{r_j^{\lambda_{Ij}^{(k)}} \Psi_{Iij}(\theta_j, \lambda_{Ij}^{(k)})\} \tag{55}$$

The $\hat{\ }$-symbol denotes that the vertex-intensity factors apply for a single normalized vertex eigenfunction $W^{(m)}(\phi,\theta)$.

The reciprocity theorem applied is (using the labelling of subsurfaces shown in Figure 6b)

$$\int_{\Gamma_3} (^{(1)}u_i \times {}^{(2)}T_i - {}^{(2)}u_i \times {}^{(1)}T_i)\,d\Gamma =$$
$$-\int_{\Gamma_s} (^{(1)}u_i \times {}^{(2)}T_i - {}^{(2)}u_i \times {}^{(1)}T_i)\,d\Gamma - \int_{\Gamma_1} {}^{(1)}u_i \times {}^{(2)}T_i\,d\Gamma \tag{56}$$

By substituting u_i from equation (55) for $^{(1)}u_i$ on the left hand side of equation (56) and using the extraction function given by equation (54) the following explicit expression for the unknown vertex-edge intensity factor is obtained

$$\rho_u^{(\Lambda^{(m)} - \lambda^{(k)} + 1)} \cdot \hat{s}_{Ij}^{(m,k)} \cdot \beta =$$
$$-\int_{\Gamma_s} (^{(1)}u_i \times {}^{(2)}T_i - {}^{(2)}u_i \times {}^{(1)}T_i)\,d\Gamma - \int_{\Gamma_1} (^{(1)}u_i \times {}^{(2)}T_i\,d\Gamma \tag{57}$$

where ρ_u is length of cone and β is given by equation (43). The extraction procedure described may be used for all (m,k) satisfying

$$\Lambda^{(m)} - \lambda_{Ij}^{(k)} + 1 \geq 0 \tag{58}$$

The technically most important vertex-edge intensity factors are for $k=1$ (order 1 edge intensity function). Since $\Lambda^{(m)} > -1/2$ and $\lambda_{Ij}^{(1)} > 0$ the equation (58) apply to this case.

The vertex intensity factors sought in equation (53)) are obtained from

$$S_{Ij}^{(m,k)} = S^{(m)} \; \hat{S}_{Ij}^{(m,k)} \tag{59}$$

We finally remark that the extraction functions equation (54) may be modified along lines discussed in Section 7 (see equations (45) to (48)).

10 Model problems

Three problems are studied in order to exemplify the convergence rate and the accuracy obtainable when employing the above extraction procedures.

The first example treats the problem of a flat elliptical crack (major and minor ellipse axes are a=2 and b=1 respectively) in an infinite space of elastic material (ν=0.3). Uniform remote tensile stresses σ_z=1 and τ_{xz}=1 are applied (Figure 7). An analytical solution to this problem is given in [18]. The edge intensity functions,

$$K_I^{(1)} = \frac{\sigma_z}{\Phi} \left(\frac{\pi b}{a}\right)^{1/2} \left(a^2 \sin^2 t + b^2 \cos^2 t\right)^{1/4} \tag{60}$$

$$K_{II}^{(1)} = \frac{-4GA_1}{a^2} \tau_{xz} \left(\frac{\pi a}{b}\right)^{1/2} \left(a^2 \sin^2 t +\right.$$
$$\left. b^2 \cos^2 t\right)^{-1/4} \times \cos t \tag{61}$$

$$K_{III}^{(1)} = \frac{-4GA_1(1-\nu)}{b^2} \tau_{xz} \left(\frac{\pi b}{a}\right)^{1/2} \left(a^2 \sin^2 t +\right.$$
$$\left. b^2 \cos^2 t\right)^{-1/4} \times \sin t \tag{62}$$

in which, A_1(a/b,ν) is a constant and Φ is the elliptic integral of second kind are generally nonzero along the edge.

In the numerical analysis, a cube-shaped domain with side lengths 30b enclosing the elliptical crack is studied. The analytical solution is used to calculate consistent forces in the finite element analysis. Thus an exact solution to the model example is available.
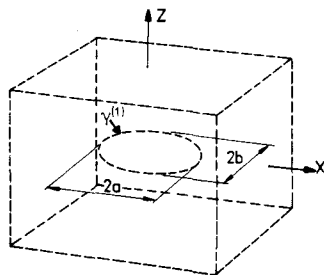
Figure 7   Embedded elliptical crack in infinite space subject to remote uniform stresses σ_z=1 and τ_{xz}=1. Dimension of crack is a/b=2

Figure 8 shows the FE-mesh used in the analysis. The mesh may be considered to consist of the parts A and B. Part A consists of three layers of elements where in each plane the coarsest possible grading in the direction along the crack fronts has been used. Part B is cylindrical mesh (outer radius is ρ_u=0.15b) with the elliptical crack front as cylinder axis (compare domain "B" in Figure 5). The mesh in part B is characterized by the number of radial layers m and the grading factor α. The total number of (brick-shaped and wedge-shaped) finite elements in the mesh is (4m+18).
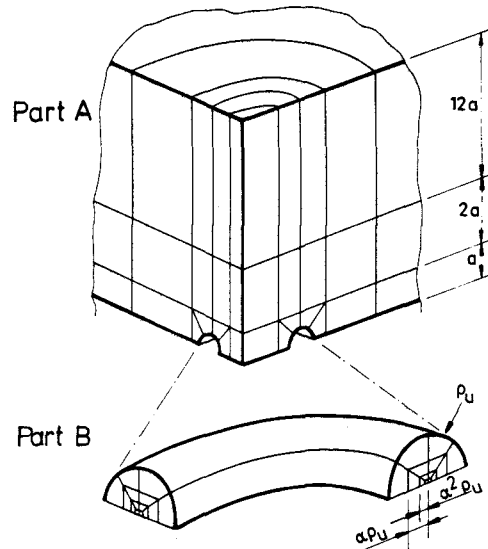
Figure 8   Principal mesh used for analysis of elliptical crack

The mesh shown in Figure 8 is not optimal. The mesh in part A is a mesh which is easy to prepare using one of the many standard FE-preprocessors available. Close to the edge the mesh design is characteristic for the h-p version of the finite element method. The elements inside the cylinder have aspect ratios of the order 10 to 10^4. Such elements have to be generated automatically since it is not possible to inspect such a mesh visually.

It is possible to construct a mesh generator which, based on an existing coarse mesh, automatically replaces finite elements connected to specified edges and vertices with sets of strongly graded cylindrical and spherical meshes. One such meshgenerator has been implemented in the code STRIPE which is used to derive numerical results in the present paper. This type of mesh generator is much simpler to implement than is a general mesh-generator for the h-p version of FEM. The mesh generation concept is successful due to the fact that optimal meshes indeed should be very strongly graded towards edges and vertices where the exact solution is singular [4,19]. By increasing the order of approximation p in the entire mesh while keeping the user-supplied part of the mesh fixed and simultaneously refining the mesh close to vertices and edges an exponential

rate of convergence in engineering quantities still may be obtained.

Consider the error in computed edge intensity functions. The error is defined as

$$\max_{t\in[0,\pi/2]} \left| \frac{K_I^{(1)} - \tilde{K}_I^{(1)}}{K_I^{(1)}} \right| \quad ,$$

$$\max_{t\in[0,\pi/4]} \left| \frac{K_{II}^{(1)} - \tilde{K}_{II}^{(1)}}{K_{II}^{(1)}} \right| \quad \text{or}$$

$$\max_{t\in[\pi/4,\pi/2]} \left| \frac{K_{III}^{(1)} - \tilde{K}_{III}^{(1)}}{K_{III}^{(1)}} \right| \quad (63)$$

where the tilda-symbol (~) denotes the finite element solution. The crack front is defined by $X_e = a \cos(t)$, $Y_e = b \sin(t)$ and $z=0$.

Figure 9 shows the error in computed edge intensity function $K_I^{(1)}$ as function of order of approximation p. The load system is $\sigma_z = 1$.

Order of approximation p

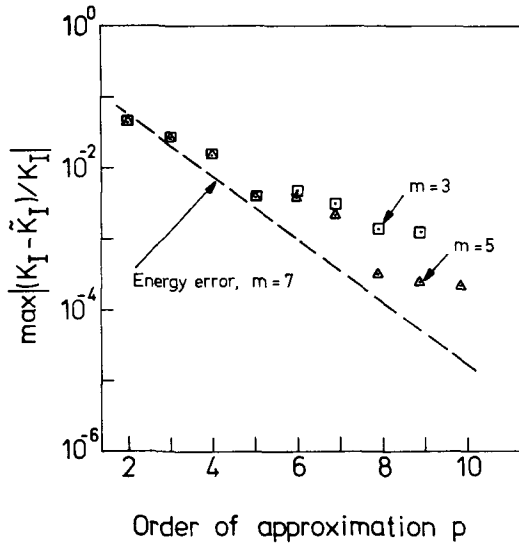Figure 9   Maximum relative error in $K_I^{(1)}$ as function of polynomial order of approximation p used

In figure 10 the error in mode II and mode III edge intensity funtions $K_{II}^{(1)}$ and $K_{III}^{(1)}$ are plotted for the loading case $\tau_{xz} = 1$.

The results shown in figures 9 and 10 exemplifies that, it is possible to derive *pointwise* values of the edge intensity functions K_I, K_{II} and K_{III} with very high accuracy. Use of the h-p version of the finite element method combined with the extraction procedures discussed in section 7 leads to a strong and in this case
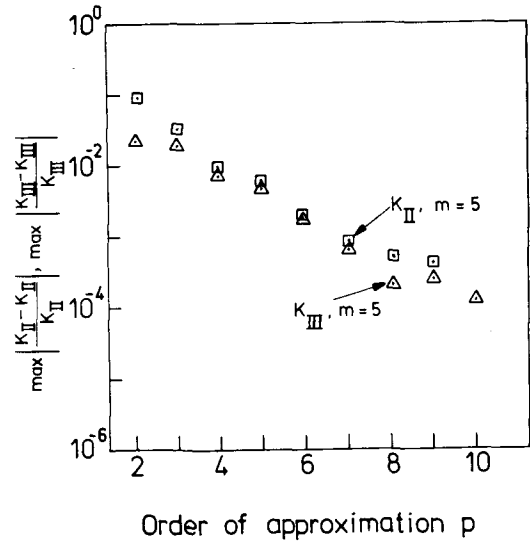
Order of approximation p

Figure 10   Maximum relative error in $K_{II}^{(1)}$ and $K_{III}^{(1)}$ as function of polynomial order of approximation used.

nearly monotonic rate of convergence. The rate of convergence is approximatively *exponential* up to a certain *p*-level which is determined by the number of layers *m* of element in part B of the mesh. The computational procedure thus *is efficient* and *reliable*. The finite element mesh used has only one finite element along the entire crack front. This obviously is not a limiting factor.

As a second example we consider the main frame fuselage studied in [20]. Figure 11 shows a finite element mesh used for damage tolerance assessment of the fuselage. The mesh was designed for the h-version of the finite element method.
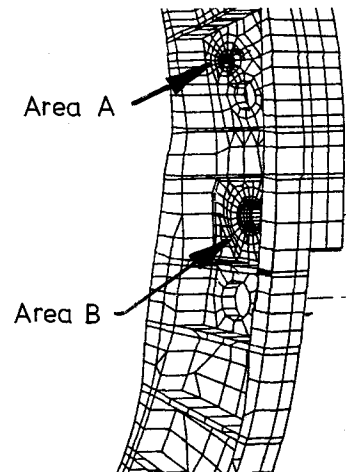
Figure 11 FE-mesh of main frame fuselage for h-version of finite element method

For the damage tolerance assessment edge intensity functions for a quarter-circular crack located in area B at the boundary of a bolt hole in the web are needed. The load transfer from bolt

to the web of the fuselage is very complex (for
more details see [20]). The analysis was performed
in the following way. The mesh available which was
nearly uniform was modified in the most simple way
by just introducing a cylindrical mesh of the type
shown in Figure 8 (part B) and adjusting a few
elements attached to this cylinder. The mesh in-
side the cylinder has four radial layers ($m=4$) of
element and two layers of element along the crack
front. The details of the solution close to the
ends of the crack front (at the vertices) is not
revealed with this mesh.

Solutions for uniform $p=2,3...7$ were obtained.
Figure 12 shows the calculated maximum values of
K_I close to the ends of the crack front as func-
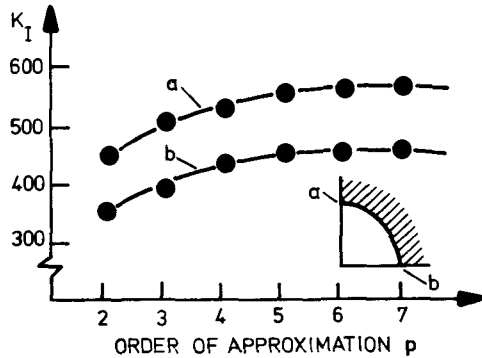tion of order of approximation p used.

Figure 12 Calculated values of K_I close to
ends of crack front for different
orders of approximation p used

The Figure shows that for $p>4$ solutions have
from a practical point of view converged. This
practical application exemplifies that methods
developed in the present paper may be used to effi-
ciently derive *reliable* engineering solutions to
complex problems.

We remark that the p-version and the h-p ver-
sion of the finite element method gives very
accurate solutions in areas where the exact solu-
tion is smooth. Consider as an example the *maximum
stress* at a fuel tube hole in the fuselage (area A
in Figure 11). Figure 13 shows the calculated max-
imum stress as function of maximum order of
approximation used when employing the self-
adaptive solution scheme described in Section 6
(for details see [10]). Again we note that we seem
to have a well-converged solution for $p \geq 4$.

In example three we demonstrate the computa-
tion of vertex and vertex-edge intensity factors
by studying the cube-shaped domain shown in Figure
1. In order to exemplify the reliability of the
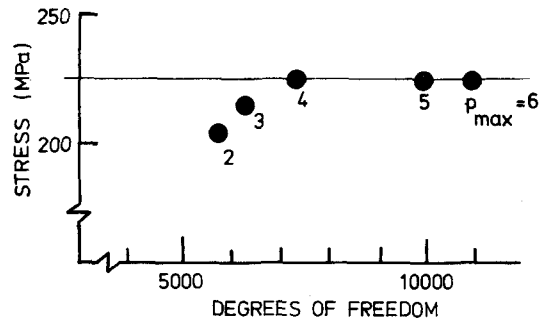numerical schemes an exact analytical solution is
needed.

Figure 13 Calculated maximum stress at fuel-
tube hole in fuselage

The displacement solution,

$$u_1 = 0$$

$$u_2 = 0 \tag{64}$$

$$u_3 = \rho^\Lambda (\sin\phi)^{1/2} \cos\phi \sin((\pi-\theta)/2)$$

with $\Lambda = 3/2$, $R = (x^2+y^2+z^2)^{1/2}$, $\theta = atan(-x/z)$ and
$\phi = atan((x^2+z^2)^{1/2}/y)$ will be used for this pur-
pose.

The function u_3 is harmonic and with Youngs
modulus $E=1$, shear modulus $G=1$ and Poissons ratio
$v=0$ it satisfies Navier equations with boundary
conditions

$$u_3 = 0 \quad \text{on the face } y=0$$

$$u_3 = 0 \quad \text{on the face } x=0, \ z \geq 0 \tag{65}$$

The volume force density is $X_3=0$ in the entire
domain. Tractions on the three faces $x=a$, $y=2a$ and
$z=-a$ is derived from equations (1-4) and equations
(64).

It would of course be preferable to have a
more general test case. It is however unlikely
that such solutions exist in the analytical form
(see for example [9,21,22]) necessary to express
the true error in calculated intensity parameters.

The solution (64) exhibits the standard square
root singularity along the edge $\gamma^{(1)}$ (the crack
front). At vertex $A^{(1)}$ the solution (64) may be
decomposed (equation (21)) as

$$u_3 = S \times \rho^\Lambda \times \psi_0(\theta,\phi) +$$
$$s_1 \times \chi(r_y) \times y^{(\Lambda-\lambda_1)} \times r_y^{\lambda_1} \psi_1(\theta) + \tag{66}$$
$$s_3 \times \chi(r_z) \times z^{(\Lambda-\lambda_3)} \times r_z^{\lambda_3} \psi_3(\theta,\phi)$$

where r_y and r_z are distances to the x- and z-axes
respectively. The scalar S is the vertex intensity
factor for vertex $A^{(1)}$; s_1 and s_3 are the vertex-
edge intensity factors for the edges $\gamma^{(1)}$ and $\gamma^{(3)}$
terminating at vertex $A^{(1)}$.

1743

For the boundary conditions (65) the eigen-values are

$$\lambda_1 = 1/2, \qquad \lambda_3 = 2 \qquad (67)$$

Note that equations (16) gives edge eigenvalues for traction free boundary conditions. The eigenvalues (67) for this example are roots to $\sin(\omega^{(j)}\lambda) = 0$.

The smooth functions $\psi_1(\theta)$ and $\psi_3(\phi, \theta)$ are

$$\psi_1 = \sin((\pi - \theta)/2) \qquad (68)$$

$$\psi_3 = \sin(2\phi)\sin(\pi - \theta)/(\cos^2\phi + \sin^2\phi \sin^2(\pi - \theta))$$

The function ψ_0 is $(\sin\phi)^{1/2}\cos\phi \sin((\pi - \theta)/2)$ except in the neighbourhood of the three edges.

The analytical values for the intensity factors are (factor $\sqrt{2\pi}/G$ is omitted)

$$S = 1$$

$$s_1 = 1$$

$$s_2 = 1/4 \qquad (69)$$

The edge intensity function is $K(y) = y$.

We use the extraction procedures discussed in Sections 7,8 and 9 to derive numerical solutions to this test problem. The edge intensity factor computation proceeds as for model problem one. The shape of the domain Ω^e is of type 'E' shown in Figure 5.

For the degenerated case considered here the extraction function for the vertex intensity factor is known analytically to be $\psi_0(\phi, \theta)$. In all practical cases however the extraction functions must be determined numerically.

In this this test problem we use the analytically determined extraction function. If vertex intensity parameters can be used to predict crack nucleation, crack growth and/or unstable fracture in practical situations it is likely that for technically important configurations and materials very accurate solutions for the eigen/extraction functions will be precomputed and stored in databases.

The FE-mesh used is shown in Figure 14. The mesh has four layers of elements strongly graded towards the edge $\gamma^{(1)}$ and the vertex $A^{(1)}$. In all 56 brick-shaped elements are used.

First, solutions for uniform p=2,3..8 are derived. The Figure 15 shows the relative error in different intensity parameters.
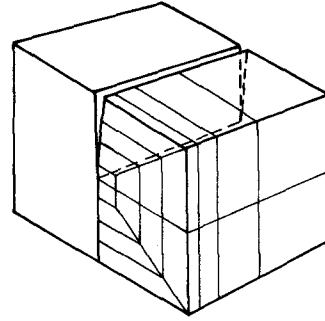

Figure 14   FE-mesh used for calculation of vertex and edge intensity parameters

The relative error in edge intensity function is defined as (the interval is selected as to avoid the singular point y=0 where K(y)=0)

$$\max_{y \in [\alpha^3 a, a]} \left| \frac{K(y) - \tilde{K}(y)}{K(y)} \right| \qquad (70)$$

The results in Figure 15 are very accurate. The rate of convergence in K, S and s_1 is of the same order as the rate of convergence in energy $(||e||_E^2)$. The maximum relative error appear for small y (where K(y) is small). If the y-interval in the error measure (70) is modified to $[\alpha^2 a, a]$ the error decrease by almost one order of magnitude.
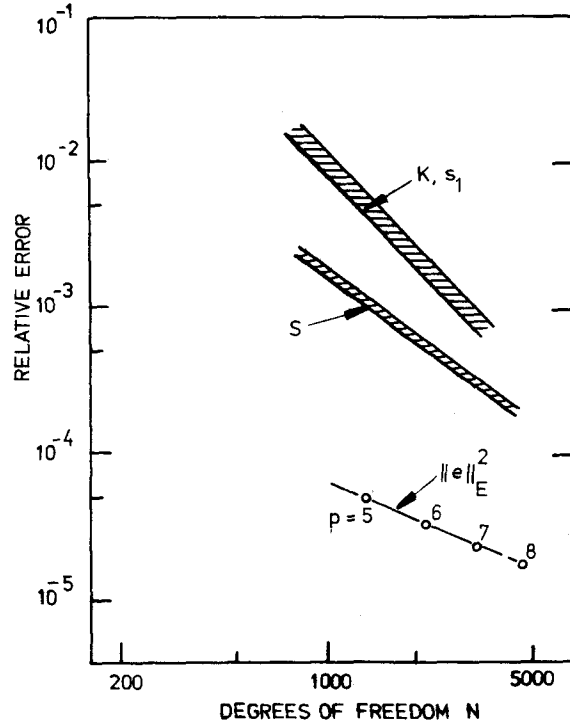

Figure 15   Error in edge intensity function K(y) and vertex intensity factor S and vertex-edge intensity factor s_1

We consider also the efficiency of the self-adaptive scheme described in Section 6. Figure 16 shows the error in calculated intensity parameters as a function of the number of degrees of freedom N used.

Solutions have been derived for $p_{max} = 2,...12$. A uniform order of approximation p=12 corresponds to 494 basis functions (equation 24) or 1482 degrees of freedom per element in a general three-dimensional case. For comparison the results obtained by using uniform p-extensions (Figure 15) are included.
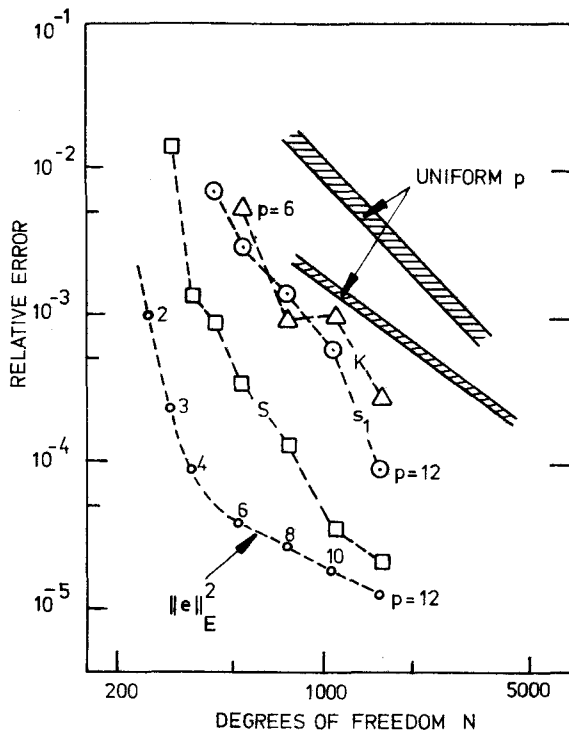

Figure 16 Error in calculated intensity parameters K, S and s_1 when a self-adaptive scheme is used

We observe that the rate of convergence is very high and that convergence is almost monotonic. The error in computed intensity parameters can be made very small (at least one or two orders of magnitude smaller than needed in any engineering application).

The efficiency (measured in number of degrees of freedom) of using non-uniform p-distributions (the self-adaptive scheme) as compared to using uniform p-extension is clearly demonstrated. The number of degrees of freedom, however, is a simple but not always relevant measure. Better efficiency measures include the required CPU-time, wall-clock time, central memory and disc storage sizes. The computational efficiency also will strongly depend on the architecture of the computer computer used (e.g single-processor super computer, massive parallel computer etc).

If CPU-time is used as a measure, the self-adaptive scheme requires on a CRAY-XMP (single processor) much less CPU-time for a requested accuracy (factors three to five). In a more practical case, for example, when deriving data in Figure 13 (for details see [10]) the self-adaptive scheme requires 5-6 times shorter CPU-time than did the uniform scheme.

It seems that use of advanced extraction methods, self-adaptive schemes and simple mesh generators as demonstrated above are effective and provide a computational tool for easy extraction of all engineering quantites of interest in an accurate and reliable way.

11. Concluding remarks

The prediction of slow crack growth of flaws in three-dimensional aircraft components are generally based on linear elastic fracture mechanics analyses. Currently used crack propagation "laws" require as input, stress intensity factors as function of crack size and crack shape. The main objective with the stress analysis in case of damage tolerant dimensioning is to provide reliable data for stresses and stress intensity factors to a minimum cost (manpower cost and computer cost).

The procedures developed here do provide accurate values for parameters characterizing the exact matematical solution. Error estimates of the type given by equations (23,33) are (and should be) with respect to the well defined mathematical problem. The displacement distributions in aircraft components, however, do not satisfy exactly the Navier equations. Different corrections of the solution are sometimes needed in applications (for example introduced in crack propagation "laws"). It is therefore very essential that the numerical solutions used to evaluate experimental data contain only small errors in the norms we discuss (that is with respect to the mathematically exact solution). The reason is that corrections introduced really must reflect the influence of material nonlinearities, load sequence effects etc and not a poor analytical procedure. It is reasonable to expect that the large scatter often observed when comparing numerical-experimental crack propagation data in three-dimensional situations largely is due to a poor analytical procedure.

For analysis of complex frames of the type shown in Figure 11, the error in stress intensity factor data if estimated from handbooks may (in sections with complex geometry and load distribution) be of the order, say, be 20-50%. Such uncertainties require a large conservatism which leads to a considerably weight penalty. By applying the computational procedure discussed in the present paper it is possible to derive all linear elastic fracture mechanics parameters of interest in a simple and reliable way. The main fuselage frame analysed in section 10 exemplify that the advocated procedures are for practical use.

12. References

[1] Babuška I, "The p- and h-p versions of the finite element method. The state of the art". Technical Note BN-1156, Inst for Physical Science and Technology, University of Maryland, Maryland, Sept 1986 to appear in Proceeding of finite element Workshop, edited by R Voigt Springer-Verlag 1987

[2] Babuška I and Dorr M, "Error estimates for the combined h- and p- versions of the finite element method", Num Math, Vol 37, 1981, pp.257-277

[3] Babuška I and Guo B Q, " The h-p version of the finite element method for domains with curved boundaries", SIAM J Num Anal, Vol 25, No 4, 1988, pp.837-861

[4] Babuška I and Guo B Q, "The h-p version of finite element mehtod, Part 1: The basic approximation results, Comp.Mech., 1 (1986), pp.203-220

[5] Tobias von Petersdorff, "Randwertprobleme der Elastizitätstheorie für Polyeder-Singularitäten und Approximation mit Randelementmethoden", Dissertation, Darmstadt 1989

[6] Kondrat'lev V A, "Boundary problems for elliptic equations in domains with conical or angular points", Trans Moscow Math Soc Vol 16 1967, pp.227-313

[7] MIL-A-83444 (USAF), Military Specification. Airplane Damage Tolerance Requirements. July 1974

[8] Blom A and Andersson B, "On the semi-elliptical surface crack problem: Detailed numerical solutions for complete elastic stress fields", FFA Technical note FFA TN 1988-74, Stockholm 1988

[9] Benthem J P, "State of Stress at the Vertex of a Quarter-Infinite Crack in a Half-Space", International Journal of Solids And Structure, Vol.13, 1977, pp.479-492.

[10] Andersson B and Falk U, "Self-Adaptive Analysis of Three-Dimensional Structures using a p-Version of Finite Element Method". Stockholm, 1986. Accepted for publication in Computers and Structures.

[11] Peano A, "Hierarchies of conforming finite elements", Thesis, Washington University, St. Louis, 1975

[12] Kelly D W, Gago J P, Zienkiewitcz O, and Babuska I, Aposteriori error analysis and adaptive processes in the finite element method:
Part I - Error analysis, Int J for Numerical Methods in Engineering, Vol 19, 1983, pp 1593-1620

[13] Peano A, Fanelli M, Riccioni R and Sardella L, "Selfadaptive convergence at the crack tip of a dam buttress, Int Conf Num Meth in Fracture Mech, Svansea, 1979

[14] Babuška I and Osborn J E, "Estimate for the Errors in Eigenvalue and Eigenvector Approximation by Galerkin Methods, with Particular Attention to the Case of Multiple Eigenvalues", Technical Note BN-1056, Institute for Physical Science and Technlolgy, University of Maryland, College Park, Maryland, Nov. 1986.

[15] Gordon W J and Hall C A , "Transfinite Element Methods: Blending-Function Interpolation over Arbitrary Curved Element Domains", Numerishe Mathematik, 21, pp.109-129, 1973.

[16] Babuška I and Miller A, "The postprocessing Approcah in the finite element method - part 1: Calculation of displacements, stresses and other higher derivatives of the displacements", Int Journal for Num Methods in Engineering, Vol 20, 1984, pp.1085-1109

part 2: "The calculation of stress intensity factors", Int Journal for Num Methods in Engineering, Vol 20, 1984, pp.1111-1129

part 3: "Aposteriori error estimates and adaptive mesh selection", Int Journal for Num Methods in Engineering, Vol 20, 1984, pp.2311.2324

[17] Szabo B A and Babuška I , "Computation of the amplitude of stress singular terms for cracks and reentrant corners", Report WU/CCM-86/1, Washington University, St Louis, 1986

[18] Kassir M K and Sih G C, "Three-dimensional stress distribution around an elliptical crack under arbitrary loading", Trans ASME J Appl Mech, 1966, pp.601-611.

[19] Szabo B A, "Mesh Design for the p-Version of the Finite Element Method", Report WU/CCM-85/2, Washington University, St.Louis, MO, 1985.

[20] Palmberg B, Olsson M-O, Boman P-O and Blom A, "Damage Tolerance Analysis and Testing of the Aircraft 37 Viggen. ICAS proceeding, Stockholm 1990.

[21] Bazant Z P and Estenssoro L F "Surface Singularity and Crack Propagation", International Journal of Solids and Structures, Vol.15, 1979, pp.405-426.

[22] Walden H and Kellogg R B, "Numerical Determination of the Fundamental Eigenvalue for the Laplace Operator on Spherical Domain", Journal of Engineering Mathematics, Vol. 11, 1977, pp.299-318.